Multi-Core Optical Fibers With Bragg Gratings as Shape Sensor for Flexible Medical Instruments

Fouzia Khan, Alper Denasi, David Barrera, Javier Madrigal, Salvador Sales, and Sarthak Misra

***Abstract*— This paper presents a technique to reconstruct the shape of a flexible instrument in three-dimensional Euclidean space based on data from fiber Bragg gratings (FBGs) that are inscribed in multi-core fibers. Its main contributions are the application of several multi-core fibers with FBGs as shape sensor for medical instruments and a thorough presentation of the reconstruction technique. The data from the FBG sensors are first converted to strain measurements, which is then used to calculate the curvature and torsion of the fibers. The shape of the instrument is reconstructed using Frenet–Serret equations in conjunction with the calculated curvature and torsion of the instrument. The reconstruction technique is validated with a catheter sensorized with four multi-core fibers that have FBG sensors. The catheter is placed in eight different configurations and the reconstruction is compared to the ground truth. The maximum reconstruction error among all the configurations is found to be 1.05 mm. The results show that shape sensing for flexible medical instruments is feasible with FBG sensors in multi-core fibers.**

***Index Terms*— Fiber Bragg grating, bio-medical, robotics, shape sensing, medical instrument, 3D reconstruction, multi-core optical fiber.**

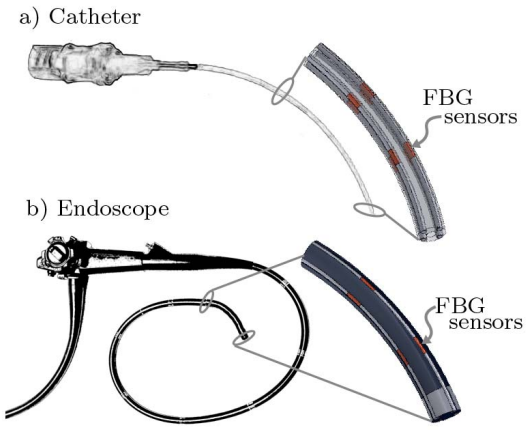

Fig. 1. Multi-core optical fibers can be placed in numerous flexible medical instruments due to their small size, flexibility, light weight, immunity to electromagnetic interference and compatibility with medical imaging modalities. Fibers with Bragg gratings (FBG) are shown embedded in (a) a catheter and (b) an endoscope.

I. Introduction

THE spatial information of a medical instrument inside the patient during a procedure is crucial for the accurate manipulation of the instrument. There exist a range of clinical applications which can benefit from the instruments spatial information, such as epidural administration, colonoscopy, biopsies, and cardiac procedures [1], [2]. Among the aforementioned applications, in the case of epidural administration procedure, a catheter is inserted into the epidural space in order to deliver drugs for pain relief. In practice, most doctors identify the epidural space based on the resistance felt through the catheter and in some cases ultrasound or fluoroscopy is utilized. However, each method has their drawbacks, the tactile feedback is very subjective, the catheter can be invisible in ultrasound images and the patient is exposed to harmful radiation in fluoroscopy [3], [4]. An alternative to these methods is to use optical sensors in the catheter for its spatial information.

Optical sensors can be used in numerous medical instruments such as endoscopes and catheters as illustrated in Figure 1. They are well suited for the medical environment, since they are small in size, flexible, lightweight, immune to electromagnetic interference and compatible with medical imaging modalities [5]. Thus, they have been utilized in numerous studies to provide feedback from medical instruments. They have been used to monitor muscle fatigue, cardiac activities and body temperature [6]–[8]. In addition, they have been applied in cardiovascular diagnosis, artery pressure detection, artery detection, intra-aortic balloon pumping, prostatic implants, and urology [1], [9]. There are also many patents on medical instruments that use these sensors [10]–[13]. Particularly, FBG sensors are used as force sensors to recognize the interface between different tissues in order to aid in accurately placing a catheter in the epidural space [14]. They have also been used to display the shape of a colonoscope and the shape of a needle in real-time [2], [15]. Moreover, FBG sensors have been applied to many different shape sensing applications. They have been used for 3D shape recognition of solid objects, shape recognition of flexible morphine wing and curvature detection of a continuum manipulator [16]–[18].

Manuscript received November 6, 2018; revised March 11, 2019; accepted March 11, 2019. Date of publication March 14, 2019; date of current version June 19, 2019. This work was supported in part by the European Union's Horizon 2020 Research and Innovation Programme under Grant 688279 (EDEN2020) and in part by the Spanish Ministry of Economy and Competitiveness under Project DIMENSION TEC2017-88029-R. The associate editor coordinating the review of this paper and approving it for publication was Dr. Ioannis Raptis. *(Corresponding author: Fouzia Khan.)*

F. Khan, A. Denasi, and S. Misra are with the Surgical Robotics Laboratory, Department of Biomedical Engineering, University of Groningen, University of Medical Center Groningen, 9713 GZ Groningen, The Netherlands, and also with the Department of Biomechanical Engineering, Faculty of Engineering Technology, University of Twente, 7522 NB Enschede, The Netherlands (e-mail: f.khan@utwente.nl).

D. Barrera, J. Madrigal, and S. Sales are with the ITEAM Research Institute, Universitat Politècnica de València, 46022 València, Spain.

Digital Object Identifier 10.1109/JSEN.2019.2905010

The studies presented thus far use FBG sensors in single core fiber however FBG sensors can also be present in multi-core fiber. FBGs in multi-core fiber have been shown to work as curvature sensor and 3D shape sensor [19]–[25]. Multi-core fibers are more expensive than single core fibers, whereas the cross sectional area of the shape sensor with multi-core fibers is smaller than the shape sensor with single core fibers. For certain instruments, such as the one used in this study, multi-core fibers have to be utilized due to the limited space. Moreover, in multi-core fibers the cores are mechanically coupled, the relative distance between the cores remain constant and the cores experience identical temperature. These properties make multi-core fibers more advantageous than single core fiber. Therefore, in this study, Fiber Bragg Grating (FBG) sensors written on multi-core optical fibers are used as shape sensors for flexible instruments.

This study is unique for its application of several multi-core fibers with FBGs as a shape sensor for a catheter. More specifically, four multi-core fibers are used although a single multi-core fiber with 3 or more cores that have FBG sensors is sufficient for reconstructing the shape of a flexible instrument. Redundant number of multi-core fibers increases the reliability of the sensing system against individual FBG sensor failure. A technique is presented in this article to reconstruct the catheter's center curve based on measurements from the FBG sensors on the four multi-core fibers. The technique is experimentally validated using Plexiglas plates and 3D printed rig which serve as ground truth. The theoretical framework utilized in the study is presented in Section II. This is followed by the description of the experimental setup and the corresponding shape reconstruction results in Section III. Finally, the conclusion is provided in Section IV.

II. Theoretical Framework

This section presents the theoretical framework utilized to reconstruct the shape of a catheter sensorized by four fibers inscribed with FBG sensors. The shape of the catheter is characterized by its center curve that is described in Section II-C. The proposed reconstruction technique consists of the following four steps. First, the strain on each fiber is calculated using the measurements obtained from the FBG sensors, as presented in Section II-A. Next, the curvature and the torsion of each fiber is calculated using those strains, Section II-B. Then, the curvature and torsion of the catheter's center curve is determined based on the four fibers' curvature and torsion, Section II-C. Lastly, the catheter's center curve is determined using the calculated curvature and torsion in conjunction with the Frenet-Serret equations in Section II-C.

A. Strain Calculation Based on FBG Sensors

The strain on an individual fiber can be calculated at discretized locations where the FBG sensors are present. An FBG is a periodic or quasi-periodic modulation of the refractive index of the fiber core. This perturbation causes light to be coupled from the incident core mode to the core mode propagated in the opposite direction [26]. Thus, part of the light spectrum is reflected back and the wavelength at which the reflection is the highest is called the Bragg wavelength, $\lambda_B \in \mathbb{R}_{>0}$. Figure 2 illustrates an FBG sensor and its working principle.

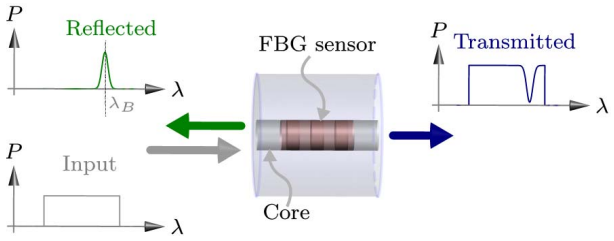

Fig. 2. A fiber Bragg grating (FBG) sensor reflects back a certain range of wavelength, $\lambda \in \mathbb{R}_{>0}$ for a given input and transmits the rest. The Bragg wavelength $\lambda_B \in \mathbb{R}_{>0}$ is the wavelength at which the power $P \in \mathbb{R}_{\geq 0}$ of the reflected spectrum is the highest.

If the FBG sensor experiences strain or change in temperature, then the Bragg wavelength, λ_B, is shifted. The Bragg wavelength is related to the applied strain and temperature as follows [27]:

$$\frac{\mathrm{d}\lambda_B}{\lambda_B} = S\mathrm{d}\epsilon + \Sigma\mathrm{d}T, \tag{1}$$

where $S \in \mathbb{R}$ is the gauge factor and $\Sigma \in \mathbb{R}$ is the temperature sensitivity. The differentials $\mathrm{d}\lambda$, $\mathrm{d}\epsilon$ and $\mathrm{d}T$ are of the wavelength, strain and temperature, respectively. Integrating (1) results in:

$$\ln \frac{\lambda_B}{\lambda_{B0}} = S(\epsilon - \epsilon_0) + \Sigma(T - T_0), \tag{2}$$

where $\epsilon \in \mathbb{R}$ is the strain, $T \in \mathbb{R}$ is the temperature and $\lambda_{B0} \in \mathbb{R}_{>0}$ is the reference Bragg wavelength at the reference strain $\epsilon_0 \in \mathbb{R}$ and reference temperature $T_0 \in \mathbb{R}$. The change in strain and temperature are related to the FBG sensor measurements by (2). This relation can be used to obtain the strain when the temperature remains constant i.e. $T = T_0$ and the reference strain (ϵ_0) along with the reference Bragg wavelength (λ_{B0}) are known.

B. Shape Reconstruction for a Single Multi-Core Fiber

The shape of a fiber is reconstructed using the curvature and torsion parameters which can be calculated from the strains on the fiber [28]. The fibers used in this study have four cores with multiple sets of FBG sensors. A section of the fiber in pure bending and a set of FBG sensors are shown in Figure 3. A set consists for four FBG sensors that are co-located and have the same reference wavelength. The sensor sets are distributed along the length of the fiber, $L \in \mathbb{R}_{>0}$. The location of the sets on the fiber and other associated quantities such as strains are parametrized using the arc length parameter, $s \in \mathbb{R}$ defined in the interval $\Omega \subset \mathbb{R}$ with $\Omega = (0, L)$. The arc length is defined for the neutral axis of the fiber. The relation between the strain ϵ_i on an FBG sensor in core i and the curvature κ is based on mechanics of a bending beam presented in Chapter 6.3 of [28]. The relation is given as:

$$\epsilon_i(s) = -\kappa(s)y_i(s) = -\kappa(s)r_i\cos(\theta_i(s)), \tag{3}$$

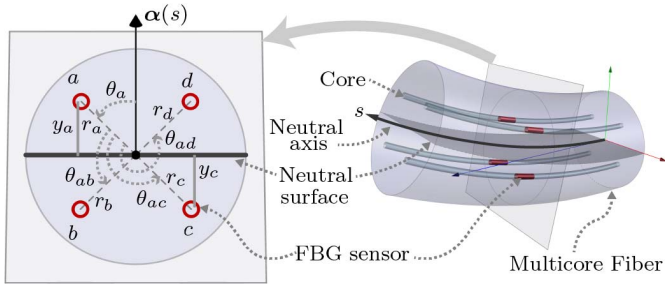

Fig. 3. Multi-core fiber with one set of fiber Bragg grating (FBG) sensors. The arc length of the neutral axis is represented with the variable $s \in \mathbb{R}$ defined in the interval $\Omega \subset \mathbb{R}$ with $\Omega = (0, L)$. The index i for the cores are a, b, c and d, respectively. At a given cross-section with FBG sensors, the curvature direction vector $\boldsymbol{\alpha}(s)$ is orthogonal to the neutral surface. The angle between $\boldsymbol{\alpha}(s)$ and core a is θ_a, whereas the angles between core a and the other cores are θ_{ab}, θ_{ac} and θ_{ad}, respectively. The radial distance from the center of the fiber to the center of the cores are labeled as r_a, r_b, r_c and r_d, respectively. The perpendicular distance from the neutral surface to the cores a and c are y_a and y_c, respectively.

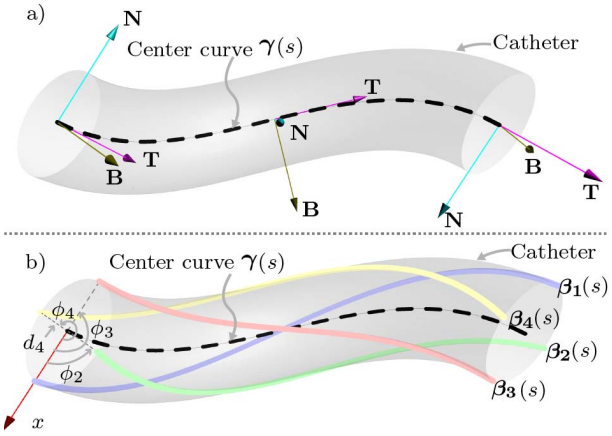

Fig. 4. (a) The center curve of the catheter with the Frenet-Serret frames. (b) Catheter with four multi-core fibers where each fiber is represented with a curve $\boldsymbol{\beta}_1 : \Omega \to \mathbb{R}^3$, $\boldsymbol{\beta}_2 : \Omega \to \mathbb{R}^3$, $\boldsymbol{\beta}_3 : \Omega \to \mathbb{R}^3$ and $\boldsymbol{\beta}_4 : \Omega \to \mathbb{R}^3$, respectively. The distance from the center of the catheter to fiber 4 is $d_4 \in \mathbb{R}_{>0}$. The angles from the reference x-axis to fiber 2, 3, and 4 are ϕ_2, ϕ_3 and ϕ_4, respectively. The center curve of the catheter is $\boldsymbol{\gamma}(s)$ where s is the arc length parameter of the curve.

where $\epsilon_i : \Omega \to \mathbb{R}$ is the strain, $\kappa : \Omega \to \mathbb{R}$ is the curvature and $i \in \{a, b, c, d\}$ is the index of the four cores. Further, $y_i : \Omega \to \mathbb{R}$ is the orthogonal distance between the neutral surface and the FBG sensor on core i, $r_i \in \mathbb{R}_{>0}$ is the radial distance from the center of the fiber cross-section to the FBG sensor on core i and $\theta_i : \Omega \to (-\pi, \pi]$ is the angle between the curvature direction vector $\boldsymbol{\alpha} : \Omega \to \mathbb{R}^3$ and r_i (see Figure 3). The curvature direction $\boldsymbol{\alpha}(s)$ in this study is a unit vector that lies on the plane of a fiber cross section. Further, it is orthogonal to the neutral surface and it points towards the compressed region of the cross section.

The measurement $\epsilon_{i_m} : \Omega \to \mathbb{R}$ from the FBG sensor in core i includes the effects of both the change in strain and temperature experienced by the FBG sensor. According to (2) the measurement $\epsilon_{i_m}(s)$ is

$$\epsilon_{i_m}(s) = S_i(\epsilon_i(s) - \epsilon_{i0}) + \Sigma_i(T(s) - T_0(s)), \tag{4}$$

where the subscript m denotes a measurement. Substituting (3) in (4) results in

$$\epsilon_{i_m}(s) = S_i(-\kappa(s) r_i \cos(\theta_i(s)) - \epsilon_{i0}) + \Sigma_i(T(s) - T_0(s)). \tag{5}$$

In the following derivations, it is assumed that the term $\Sigma_i(T(s) - T_0(s))$ in (5) is the same for all the four cores due to the close proximity of the cores. For the ease of the following derivations, the term $\Sigma_i(T(s) - T_0(s))$ is represented by a new variable $\epsilon_t(s)$. In addition, by selecting the reference strain to be zero the following equations apply to the measurements from the sensors in the four cores:

$$\epsilon_{a_m}(s) = -S_a \kappa(s) r_a \cos(\theta_a(s)) + \epsilon_t(s), \tag{6}$$
$$\epsilon_{b_m}(s) = -S_b \kappa(s) r_b \cos(\theta_a(s) + \theta_{ab}) + \epsilon_t(s), \tag{7}$$
$$\epsilon_{c_m}(s) = -S_c \kappa(s) r_c \cos(\theta_a(s) + \theta_{ac}) + \epsilon_t(s), \tag{8}$$
$$\epsilon_{d_m}(s) = -S_d \kappa(s) r_d \cos(\theta_a(s) + \theta_{ad}) + \epsilon_t(s), \tag{9}$$

where $\theta_{ab} = \frac{\pi}{2}$, $\theta_{ac} = \pi$ and $\theta_{ad} = \frac{3\pi}{2}$ for the multi-core fiber used in this study. The relations given by (6)-(9) can be represented in matrix form as follows:

$$\underbrace{\begin{bmatrix} \epsilon_{a_m}(s) \\ \epsilon_{b_m}(s) \\ \epsilon_{c_m}(s) \\ \epsilon_{d_m}(s) \end{bmatrix}}_{\boldsymbol{\epsilon}_m(s)} = \underbrace{\begin{bmatrix} -S_a r_a & 0 & 1 \\ 0 & S_b r_b & 1 \\ S_c r_c & 0 & 1 \\ 0 & -S_d r_d & 1 \end{bmatrix}}_{\mathbf{M}} \underbrace{\begin{bmatrix} \kappa(s)\cos(\theta_a(s)) \\ \kappa(s)\sin(\theta_a(s)) \\ \epsilon_t(s) \end{bmatrix}}_{\boldsymbol{\nu}(s)}. \tag{10}$$

By solving (10) for $\boldsymbol{\nu}(s)$, a solution for the angle $\theta_a(s)$ and curvature $\kappa(s)$ can be found. The solution $\boldsymbol{\nu}(s)$ from (10) can be computed as:

$$\boldsymbol{\nu}(s) = \mathbf{M}^{\dagger} \boldsymbol{\epsilon}_m(s), \tag{11}$$

where $\mathbf{M}^{\dagger}$ is the Moore-Penrose pseudo-inverse of $\mathbf{M}$. Using the relation (11), the curvature $\kappa(s)$, the torsion $\tau(s)$ with $\tau : \Omega \to \mathbb{R}$ and the angle $\theta_a(s)$ can be obtained as follows:

$$\kappa(s) = \sqrt{\upsilon_1^2(s) + \upsilon_2^2(s)}, \tag{12}$$
$$\theta_a(s) = \operatorname{atan2}(\upsilon_2(s), \upsilon_1(s)), \tag{13}$$
$$\tau(s) = \frac{\mathrm{d}\theta_a(s)}{\mathrm{d}s}. \tag{14}$$

In (12), the positive solution is selected for the curvature because the Frenet-Serret formulation assumes $\kappa > 0$. The sign of the curvature determines the direction of bending in a planar curve, however for 3D curves the torsion is used for the bending direction. The derivative operator introduced for the torsion parameter $\tau(s)$ in (14) can be numerically approximated as follows:

$$\tau(s) \approx \frac{\theta_a(s) - \theta_a(s - \Delta s)}{\Delta s} \tag{15}$$

where Δs is the difference in the arc length between the two consecutive FBG sensor sets. Consequently, the curvature and torsion for a single fiber can be found using (12) and (14) at the locations where the FBG sensor sets are present.

C. Center Curve Reconstruction for a Catheter

The curvature (12) and torsion (14) derived for an individual fiber in the previous section are used to obtain the curvature and torsion of the center curve of the catheter shown in Figure 4. In the following derivation, it is assumed that the center curve is represented as a unit speed space curve that is smooth and has a non-zero curvature along its arc length [29]. This curve can be reconstructed with the knowledge of its own curvature $\widetilde{\kappa} : \Omega \to \mathbb{R}$ and torsion $\widetilde{\tau} : \Omega \to \mathbb{R}$ parameters using the Frenet-Serret equations as follows:

$$\frac{\mathrm{d}\boldsymbol{\gamma}(s)}{\mathrm{d}s} = \mathbf{T}(s), \tag{16}$$

$$\frac{\mathrm{d}\mathbf{T}(s)}{\mathrm{d}s} = \widetilde{\kappa}(s)\mathbf{N}(s), \tag{17}$$

$$\frac{\mathrm{d}\mathbf{N}(s)}{\mathrm{d}s} = -\widetilde{\kappa}(s)\mathbf{T}(s) + \widetilde{\tau}(s)\mathbf{B}(s), \tag{18}$$

$$\frac{\mathrm{d}\mathbf{B}(s)}{\mathrm{d}s} = -\widetilde{\tau}(s)\mathbf{N}(s), \tag{19}$$

where $\boldsymbol{\gamma} : \Omega \to \mathbb{R}^3$ is the position vector, $\mathbf{T} : \Omega \to \mathbb{R}^3$, $\mathbf{N} : \Omega \to \mathbb{R}^3$ and $\mathbf{B} : \Omega \to \mathbb{R}^3$ are the tangent, the normal and the bi-normal orthogonal vectors, respectively. The relations (16)-(19) can be rewritten in matrix form as follows:

$$\frac{\mathrm{d}}{\mathrm{d}s}\mathbf{X}(s) = \mathbf{X}(s)\mathbf{A}(s), \tag{20}$$

where the pose $\mathbf{X}(s) : \Omega \to SE(3)$ and the twist $\mathbf{A}(s) : \Omega \to \mathfrak{se}(3)$ are given by:

$$\mathbf{X}(s) = \begin{bmatrix} \mathbf{R}(s) & \boldsymbol{\gamma}(s) \\ \mathbf{0}_3^T & 1 \end{bmatrix} = \begin{bmatrix} \mathbf{T}(s) & \mathbf{N}(s) & \mathbf{B}(s) & \boldsymbol{\gamma}(s) \\ 0 & 0 & 0 & 1 \end{bmatrix} \tag{21}$$

$$\mathbf{A}(s) = \begin{bmatrix} 0 & -\widetilde{\kappa}(s) & 0 & 1 \\ \widetilde{\kappa}(s) & 0 & -\widetilde{\tau}(s) & 0 \\ 0 & \widetilde{\tau}(s) & 0 & 0 \\ 0 & 0 & 0 & 0 \end{bmatrix}. \tag{22}$$

In (21), $\mathbf{R}(s) = \begin{bmatrix}\mathbf{T}(s)\ \mathbf{N}(s)\ \mathbf{B}(s)\end{bmatrix}$ with $\mathbf{R} : \Omega \to SO(3)$ describes the orthonormal frame in terms of the vectors $\mathbf{T}(s)$, $\mathbf{N}(s)$, and $\mathbf{B}(s)$ [30]. Further, $\mathbf{0}_3$ is a three dimensional vector of zeros. The aforementioned frame is illustrated at three different locations on the center curve of the catheter in Figure 4a. In order to reconstruct the center curve described by the position vector $\boldsymbol{\gamma}(s)$, the relation (20) should be solved. The solution to (20) can be obtained assuming that $\mathbf{A}(s)$ is held constant between two consecutive discretized locations on the center curve. Thus, Equation 20 can be discretized as:

$$\mathbf{X}(s + \Delta s) = \mathbf{X}(s) \exp\left(\mathbf{A}(s)\Delta s\right). \tag{23}$$

Consequently, the position vector $\boldsymbol{\gamma}(s)$ can be extracted from the last column of the solution given by (23). The center curve of the catheter described by the vector $\boldsymbol{\gamma}(s)$ and the shape of each individual fiber described by $\boldsymbol{\beta_j} : \Omega \to \mathbb{R}^3$ (see Figure 4b) are related as follows:

$$\boldsymbol{\beta_j}(s) = \boldsymbol{\gamma}(s) + d_j(-\cos(\phi_j)\boldsymbol{N}(s) + \sin(\phi_j)\boldsymbol{B}(s)) \tag{24}$$

where $j \in \{1, 2, 3, 4\}$ is the index of the fiber. Further, $d_j \in \mathbb{R}_{>0}$ is the distance from the center of the catheter to the j^{th} fiber's center and ϕ_j is the angle between the x axis and the vector from the center of the catheter to the center of the j^{th} fiber (see Figure 4b) [29]. For a given small d_j in (24), $\boldsymbol{\beta_j}(s) \approx \boldsymbol{\gamma}(s)$ holds. Consequently, the curvature and torsion calculated for the fibers can be used for the reconstruction of the center curve of the catheter.

The theoretical framework described throughout the Section II can be implemented using the Algorithms 1, 2 and 3, respectively. The following algorithms are described for the case of 6 FBG sensor sets and 118 interpolation points. However, they can be generalized to arbitrary numbers of FBG sensor sets and interpolation points.

Algorithm 1 Reconstruction of the center curve of the catheter. Input $\boldsymbol{\lambda}_i$ is a 4×6 matrix; each column is the data from one FBG set on the i^{th} fiber. Output $\boldsymbol{\gamma}$ is a 3×118 matrix that holds the 3D co-ordinates of the 118 points of the catheter's center curve. Variables $\boldsymbol{\kappa}_i$, $\boldsymbol{\tau}_i$, $\boldsymbol{\kappa}_{cath}$ and $\boldsymbol{\tau}_{cath}$ are 1×6 vectors. Variables $\boldsymbol{\kappa}_{interp}$, $\boldsymbol{\tau}_{interp}$ and $\mathbf{l}$ are 1×118 vectors. $\mathbf{X}_0$ is a 4×4 matrix

Input: $\boldsymbol{\lambda}_i$ where $i = (1, 2, 3, 4)$
Output: $\boldsymbol{\gamma}$
ReconstructCath:
for $i = 1$ to 4 **do**
  $[\boldsymbol{\kappa}_i, \boldsymbol{\tau}_i] \leftarrow$ *getShape*$(\boldsymbol{\lambda}_i)$
end for
$\boldsymbol{\kappa}_{cath} \leftarrow$ mean$(\boldsymbol{\kappa}_1, \boldsymbol{\kappa}_2, \boldsymbol{\kappa}_3, \boldsymbol{\kappa}_4)$
$\boldsymbol{\tau}_{cath} \leftarrow$ mean$(\boldsymbol{\tau}_1, \boldsymbol{\tau}_2, \boldsymbol{\tau}_3, \boldsymbol{\tau}_4)$
$\boldsymbol{\kappa}_{interp} \leftarrow$ linear interpolation $\boldsymbol{\kappa}_{cath}$
$\boldsymbol{\tau}_{interp} \leftarrow$ linear interpolation $\boldsymbol{\tau}_{cath}$
$\mathbf{l} \leftarrow$ points on catheter center curve at which the values of $\boldsymbol{\kappa}_{cath}$ and $\boldsymbol{\tau}_{cath}$ are interpolated
$\mathbf{X}_0 \leftarrow$ initial condition
$\boldsymbol{\gamma} \leftarrow$ *reconstruct*$(\boldsymbol{\kappa}_{interp}, \boldsymbol{\tau}_{interp}, l, X_0)$
return $\boldsymbol{\gamma}$

III. Experiments

The reconstruction technique presented in Section II is validated with experimental setup that is described in Section III-A and the results are given in Section III-B.

A. Experimental Setup

The hardware used in the experiments is shown in Figure 5. The catheter is 2.5 mm in diameter and has 4 segments that are interlocked and the segments can slide relative to each other [32]. Every segment has a channel, thus four multi-core fibers can be placed in the catheter. The fibers have four cores that are straight and in a cross sectional view of the fiber the cores fall on the corners of a 36 μm wide square. There are 6 sets of 10 mm long FBG sensors that are equally spaced over a distance of 118 mm on every fiber. A set consists of 4 FBG sensors, one on each core, with the same reference Bragg wavelength. The sets are inscribed using continuous wave frequency-doubled Argon-ion laser and a phase mask technique. The FBG sensors are simultaneously inscribed in all the cores, as a result the FBG sensors in all cores

Algorithm 2 The *GetShape* Function in Algorithm 1. Input $\boldsymbol{\lambda}$ is 4×6 matrix, each column is the data from one FBG set on the fiber. Output $\boldsymbol{\kappa}$ and $\boldsymbol{\tau}$ are 1×6 vectors, the i^{th} element is the curvature and torsion value at the i^{th} FBG set location on the fiber. The value $r_a = r_b = r_c = r_d = 25.46\ \mu$m, this is from the manufacture's datasheet for the fiber. The strain gauge factor $S_a = S_b = S_c = S_d = 0.777$ that is the default value from the interrogator's user manual [31]

Input: $\boldsymbol{\lambda}$
Output: $\boldsymbol{\kappa}$, $\boldsymbol{\tau}$
getShape:
for $j = 1$ to 6 **do**
  for $i = 1$ to 4 **do**
    $\epsilon_m(i) \leftarrow \ln \dfrac{\boldsymbol{\lambda}(i, j)}{\boldsymbol{\lambda}_{B0}(i, j)}$
  end for
  $\boldsymbol{\kappa}(j) \leftarrow$ solution to (12)
  $\boldsymbol{\tau}(j) \leftarrow$ solution to (15)
end for
return $[\boldsymbol{\kappa}, \boldsymbol{\tau}]$

Algorithm 3 The *Reconstruct* function in Algorithm 1. The inputs $\boldsymbol{\kappa}, \boldsymbol{\tau}, \mathbf{l}$ are 1×118 vectors. $\boldsymbol{\kappa}$ and $\boldsymbol{\tau}$ contain the curvature and torsion of the catheter's center curve at the arclength given in $\mathbf{l}$, respectively. $\mathbf{X}_0$ is a 4×4 matrix that holds the initial value of the catheter's center curve

Input: $\boldsymbol{\kappa}, \boldsymbol{\tau}, \mathbf{l}, \mathbf{X}_0$
Output: $\boldsymbol{\rho}$
reconstruct:
$\mathbf{X}(1) \leftarrow \mathbf{X}_0$
$\boldsymbol{\rho} \leftarrow$ the fourth column of $\mathbf{X}(1)$
for $i = 1$ to 118 **do**
  $\mathbf{A} \leftarrow \begin{bmatrix} 0 & -\widetilde{\kappa}(i) & 0 & 1 \\ \widetilde{\kappa}(i) & 0 & -\widetilde{\tau}(i) & 0 \\ 0 & \widetilde{\tau}(i) & 0 & 0 \\ 0 & 0 & 0 & 0 \end{bmatrix}$ from (22)
  if $i > 1$ **then**
    $\delta \leftarrow \mathbf{l}(i) - \mathbf{l}(i-1)$
  else
    $\delta \leftarrow 1$
  end if
  $\mathbf{X}(i + \delta) \leftarrow \mathbf{X}(i) \exp(\mathbf{A}\delta)$ from (23)
  $\boldsymbol{\rho}(i + \delta) \leftarrow$ the fourth column of $\mathbf{X}(i + \delta)$
end for
return $\boldsymbol{\rho}$

are co-located and have the same wavelength. The reference Bragg wavelength of the FBG sensors is unique for every set. The data from the FBG sensors of one set is required for the curvature and torsion calculations. Thus, every fiber has 6locations where the curvature and torsion can be calculated. The fan-out box holds four fan-outs, each fan-out connects the 4 cores of a multi-core fiber to four single core fibers. The 16 outputs from the fan-out box are merged to 4 outputs using four 1×4 optical couplers in order to measure them using the channels of the interrogator. Lastly, the interrogator

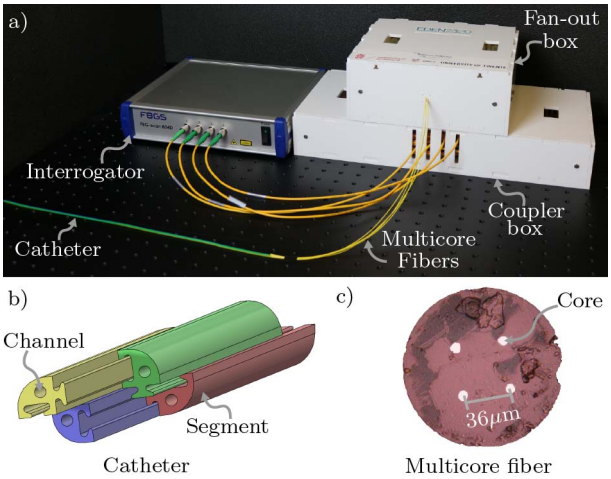

Fig. 5. (a) The experimental setup consists of an interrogator, a coupler box, a fan-out box, multi-core fibers and a multi-segment catheter. (b) The catheter consists of four segments and channels for multi-core fiber. (c) Photograph of the multi-core fiber's cross sectional view under a microscope.

TABLE I
DESCRIPTION OF THE GROUND TRUTH CONFIGURATIONS. C1 AND C2 ARE PLANAR CURVES WITH CONSTANT CURVATURE. C3 - C5 ARE PLANAR CURVES AND THE CURVATURE INCREASES LINEARLY ALONG THE ARC LENGTH. C6 - C8 ARE THREE DIMENSIONAL CURVES WITH CONSTANT CURVATURE AND CONSTANT TORSION

Config	Curvature (mm^{-1})	Torsion (mm^{-1})
C1	constant: 0.0057	constant: 0
C2	constant: 0.0020	constant: 0
C3	linearly varying: $4e^{-3}$ to $12.5e^{-3}$	constant: 0
C4	linearly varying: $4e^{-3}$ to $10e^{-3}$	constant: 0
C5	linearly varying: $4e^{-3}$ to $8.3e^{-3}$	constant: 0
C6	constant: $16.7e^{-3}$	constant: $2.77e^{-4}$
C7	constant: $14.3e^{-3}$	constant: $6.11e^{-4}$
C8	constant: $12.5e^{-3}$	constant: $3.12e^{-4}$

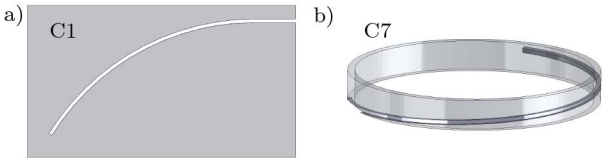

Fig. 6. Representative images of the ground truth configurations. (a) Computer Aided Design (CAD) model of configuration C1, which is a planar curve with a constant curvature of 0.0057 mm^{-1}. Configurations C1 till C5 are created by laser cutting Plexiglas plates. (b) CAD model of configuration C7, which is a curve with constant curvature of $14.3e^{-3}$ and constant torsion of $6.11e^{-4}$. Configurations C6 till C8 are 3D printed.

is the device which provides the light source and measures the reflected light from the FBGs in the fibers.

The catheter is designed by the Mechatronics In Medicine Lab (London, United Kingdom) and produced by Xograph (Stonehouse, United Kingdom). The FBG sensors are inscribed on the multi-core fiber in the iTeam lab (Valencia, Spain). The multi-core fibers and the fan-outs are from Fibercore (Southampton Science Park, United Kingdom) and the product number is FAN-4C and SM-4C1500, respectively. The optical couplers are from Newport Corporation (California, USA) with the product number F-CPL-B14350-FCAPC. The model of the interrogator is FBG-scan 840D from FBGS International NV (Geel, Belgium).

TABLE II

CATHETER RECONSTRUCTION ERRORS. $\overline{r}_e = \text{MAX}(r_e)$ AND $\overline{r}_{en} = \text{MAX}(r_{en})$ WHERE r_e AND r_{en} ARE FROM (25) AND (26), RESPECTIVELY. r_{em} IS FROM (27)

Config	C1	C2	C3	C4	C5	C6	C7	C8
$\overline{r}_e$ (mm)	0.96	0.19	0.54	0.82	1.05	0.49	0.84	0.41
$\overline{r}_{en}$ (%)	0.9	0.2	0.8	0.7	0.9	0.4	0.7	0.4
r_{em} (mm)	0.44	0.12	0.35	0.13	0.21	0.13	0.23	0.12

The catheter is sensorized by inserting four multi-core fibers into the channels of the catheter's segments and fixing the fibers at the base of the catheter. The experiments to validate the reconstruction procedure consists of placing the sensorized catheter in known configurations and observing the error between the known configuration and the reconstructed catheter shape. The values of curvature and torsion in the configurations were selected such that they are similar to the values expected in future in-vitro and ex-vivo studies. Past experiments with similar catheters show that it can take on curvatures in the range of 0.002 mm^{-1} to 0.02 mm^{-1}; thus, the curvature values within that range are selected for the configurations. The catheter is expected to have minimal torsion as a result small torsion values are used in this study [33]. Table I gives the description of the eight configurations used for validating the reconstruction procedure and the Computer Aided Design (CAD) of configurations C1 and C7 are illustrated in Figure 6.

B. Shape Reconstruction Results

The sensorized catheter is placed in all of the configurations described in Table I. For every configuration the data from the interrogator is collected and the catheter's center curve is reconstructed offline in MATLAB according to Algorithm 1. The reconstruction of the fiber and the catheter is compared to the ground truth via absolute error $r_e \in \mathbb{R}_{\geq 0}$, normalized error $r_{en} \in \mathbb{R}_{\geq 0}$ and mean error $r_{em} \in \mathbb{R}_{\geq 0}$ which is calculated as follows:

$$r_e(k) = \|\mathbf{r}_{gt}(k) - \boldsymbol{\gamma}(k)\|, \tag{25}$$

$$r_{en}(k) = \frac{r_e(k)}{k}, \tag{26}$$

$$r_{em} = \frac{1}{n}\sum_{k=1}^{n} r_e(k), \tag{27}$$

where, $k \in \mathbb{Z}_{\geq 0}$ representing the 118 points along the arc length at which the error calculation is conducted, $\mathbf{r}_{gt} \in \mathbb{R}^3$ is the ground truth curve and $\boldsymbol{\gamma}$ is the reconstruction based on proposed technique from Section II. The reconstruction and the error r_e in reconstruction over the arc length for the catheter is shown in Figure 7 and the maximum error measures $\overline{r}_e = \max(r_e)$ and $\overline{r}_{en} = \max(r_{en})$ in conjunction with the mean error for catheter is given in Table II.

The reconstruction error r_e as defined in (25) is shown in Figure 7b and 7d. The error increases with the arc length because the reconstruction is conducted by numerical integration thus the error accumulates. However, the maximum absolute error and maximum mean error in the 8 configurations is 1.05 mm and 0.44 mm, respectively. This error can be due to the difference between the catheter center curve and the configuration curve caused by placement inaccuracies during the experiments. It could also be due to misalignment in the longitudinal axis of the FBGs in the four fibers due

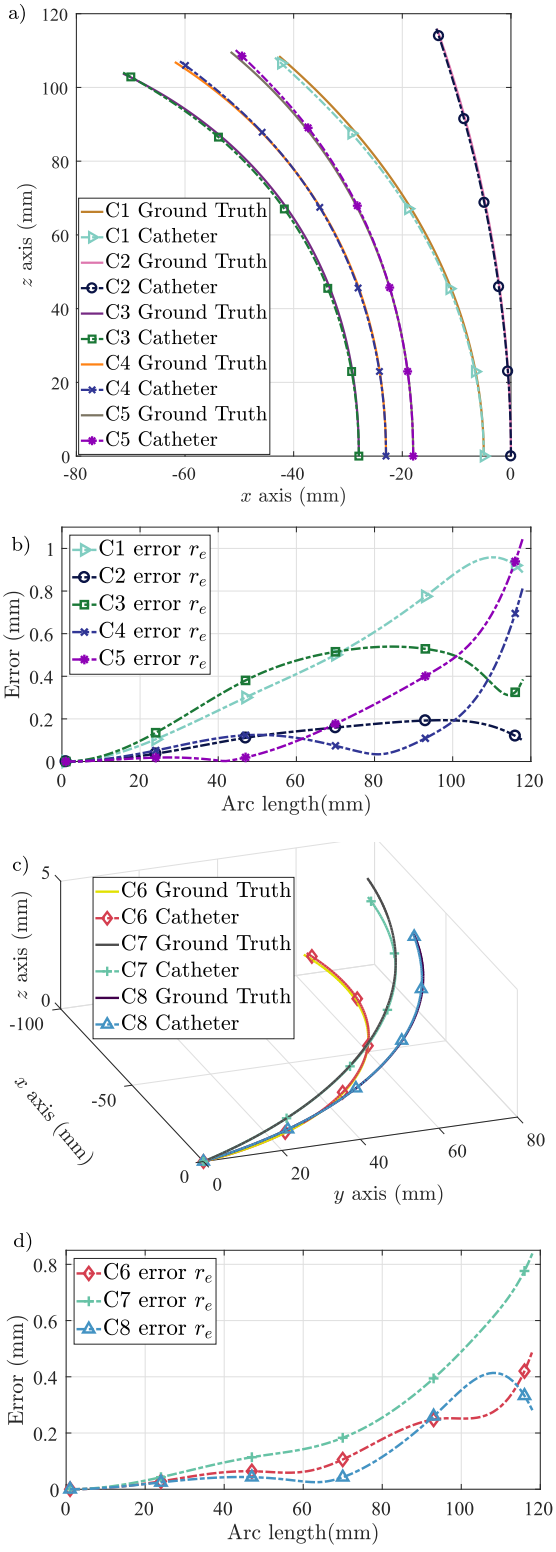

Fig. 7. (a) Reconstruction plots of the planar curves, configuration C1-C5. (b) The error r_e plot along the arc length of the catheter for the planar curves, configuration C1-C5. (c) Reconstruction plots of the 3D curves, configuration C6-C8. (d) The error r_e plot along the arc length of the catheter for the 3D curves, configuration C6-C8.

to misplacement of the fibers in the catheter. Lastly, since the fibers were not fixed along the length of the catheter the twist experienced by the catheter may not be transferred completely to the fibers.

IV. Conclusions

A shape reconstruction technique which uses redundant number of multi-core fibers with FBG sensors as shape sensor for flexible medical instruments is proposed in this work. The technique is validated on a multi-segment catheter where each segment contains a multi-core fiber with FBG sensors inscribed on it. The presence of several multi-core fibers increases the reliability of the shape sensing system against sensor failure. The proposed technique is experimentally validated for 8 different configurations where a maximum reconstruction error of 1.05 mm is observed. Further, it can be deduced that shape sensing using several multi-core fibers for flexible medical instruments is feasible.

Acknowledgments

The authors would like to thank the Mechatronics In Medicine Lab (Imperial College London) for providing the computer aided design and the samples of the catheter. They appreciate the help of Luigi Capuano (Surface technology and tribology group, University of Twente) for generating the cross sectional photograph of the multi-core fiber.

References

[1] D. Tosi, E. Schena, C. Molardi, and S. Korganbayev, "Fiber optic sensors for sub-centimeter spatially resolved measurements: Review and biomedical applications," *Opt. Fiber Technol.*, vol. 43, pp. 6–19, Jul. 2018.

[2] X. Yi, M. Wang, and X. Cheng, "Deformation sensing of colonoscope on FBG sensor net," *Indonesian J. Elect. Eng. Comput. Sci.*, vol. 10, no. 8, pp. 2253–2260, 2012.

[3] M. Nikooseresht, M. Hashemi, S. A. Mohajerani, F. Shahandeh, and M. Agah, "Ultrasound as a screening tool for performing caudal epidural injections," *Iranian J. Radiol.*, vol. 11, no. 2, 2014, Art. no. e13262.

[4] H. Gharries, "Is ultrasound guided spine injection safe," *J. Anesthesia Critical Care, Open Acesss*, vol. 10, no. 4, pp. 131–138, 2018.

[5] V. Mishra, N. Singh, U. Tiwari, and P. Kapur, "Fiber grating sensors in medicine: Current and emerging applications," *Sens. Actuators A, Phys.*, vol. 167, no. 2, pp. 279–290, 2011.

[6] D. Polito *et al.*, "A needlelike probe for temperature monitoring during laser ablation based on fiber Bragg grating: Manufacturing and characterization," *J. Med. Devices*, vol. 9, no. 4, pp. 1–29, 2015.

[7] K. Chethana, A. S. G. Prasad, S. N. Omkar, and S. Asokan, "Fiber Bragg grating sensor based device for simultaneous measurement of respiratory and cardiac activities," *J. Biophoton.*, vol. 10, no. 2, pp. 278–285, 2017.

[8] P. F. Nascimento, A. P. G. O. Franco, R. Fiorin, M. A. de Souza, H. J. Kalinowski, and I. Abe, "Case study of muscle fatigue in parafunctional patient using occlusal device with fiber Bragg grating sensors," *J. Microw., Optoelectron. Electromagn. Appl.*, vol. 17, no. 2, pp. 306–318, 2018.

[9] S. C. M. Ho, W. Li, M. Razavi, and G. Song, "Fiber bragg grating based arterial localization device," *Smart Mater. Struct.*, vol. 26, no. 6, pp. 1–10, 2017.

[10] G. W. T. Hooft, "Optical shape sensing system and method for sensing a position and/or shape of a medical device using backscatter reflectometry," U.S. Patent 20 180 128 600 A1, May 10, 2018.

[11] G. Leo, N. Aeby, and D. Inaudi, "Medical apparatus system having optical fiber sensing capability," U.S. Patent 9 907 618 B2, Mar. 6, 2018.

[12] D. K. Gifford *et al.*, "Force sensing in a distal region of an instrument including single-core or multi-core optical fiber," U.S. Patent 20 180 128 599 A1, May 10, 2018.

[13] T. Bosselmann and O. Schuetz, "Medical instrument for insertion into an examination subject, and medical examination/treatment device employing same," U.S. Patent 6 470 205 B2, Oct. 22, 2002.

[14] B. Carotenuto *et al.*, "Optical guidance systems for epidural space identification," *IEEE J. Sel. Topics Quantum Electron.*, vol. 23, no. 2, pp. 371–379, Mar./Apr. 2017.

[15] R. J. Roesthuis, M. Kemp, J. J. van den Dobbelsteen, and S. Misra, "Three-dimensional needle shape reconstruction using an array of fiber Bragg grating sensors," *IEEE/ASME Trans. Mechatronics*, vol. 19, no. 4, pp. 1115–1126, Aug. 2014.

[16] L. Xu, J. Ge, J. H. Patel, and M. P. Fok, "3-dimensional soft shape sensor based on dual-layer orthogonal fiber Bragg grating mesh," in *Proc. Opt. Fiber Commun. Conf. Exhib. (OFC)*, California, CA, USA, Mar. 2017, pp. 1–3.

[17] G. Sun, Y. Wu, H. Li, and L. Zhu, "3D shape sensing of flexible morphing wing using fiber Bragg grating sensing method," *Optik*, vol. 156, pp. 83–92, Mar. 2018.

[18] S. Sefati, M. Pozin, F. Alambeigi, I. Iordachita, R. H. Taylor, and M. Armand, "A highly sensitive fiber Bragg grating shape sensor for continuum manipulators with large deflections," in *Proc. IEEE SENSORS*, Glasgow, U.K., Oct. 2017, pp. 1–3.

[19] F. M. Araújo, L. A. Ferreira, and J. L. Santos, "Simultaneous determination of curvature, plane of curvature, and temperature by use of a miniaturized sensing head based on fiber Bragg gratings," *Appl. Opt.*, vol. 41, no. 13, pp. 2401–2407, 2002.

[20] D. Zheng, J. Madrigal, H. Chen, D. Barrera, and S. Sales, "Multicore fiber-Bragg-grating-based directional curvature sensor interrogated by a broadband source with a sinusoidal spectrum," *Opt. Lett.*, vol. 42, no. 18, pp. 3710–3713, 2017.

[21] G. M. H. Flockhart, W. N. MacPherson, J. S. Barton, J. D. C. Jones, L. Zhang, and I. Bennion, "Two-axis bend measurement with Bragg gratings in multicore optical fiber," *Opt. Lett.*, vol. 28, no. 6, pp. 387–389, Mar. 2003.

[22] J. P. Moore and M. D. Rogge, "Shape sensing using multi-core fiber optic cable and parametric curve solutions," *Opt. Express*, vol. 20, no. 3, pp. 2967–2973, Jan. 30, 2012.

[23] J. P. Moore, "Shape sensing using multi-core fiber," in *Proc. Opt. Fiber Commun. Conf. Exhib. (OFC)*, California, CA, USA, Mar. 2015, pp. 1–3.

[24] D. Barrera, I. Gasulla, and S. Sales, "Multipoint two-dimensional curvature optical fiber sensor based on a nontwisted homogeneous four-core fiber," *J. Lightw. Technol.*, vol. 33, no. 12, pp. 2445–2450, Jun. 15, 2015.

[25] A. Denasi *et al.*, "An observer-based fusion method using multicore optical shape sensors and ultrasound images for magnetically-actuated catheters," in *Proc. IEEE Int. Conf. Robot. Automat. (ICRA)*, Brisbane, QLD, Australia, May 2018, pp. 50–57.

[26] K. O. Hill and G. Meltz, "Fiber Bragg grating technology fundamentals and overview," *J. Lightw. Technol.*, vol. 15, no. 8, pp. 1263–1276, 1997.

[27] J. V. Roosbroeck, C. Chojetzki, J. Vlekken, E. Voet, and M. Voet, "A new methodology for fiber optic strain gage measurements and its characterization," in *Proc. SENSOR+TEST Conf. Opto*, Nürnberg, Germany, May 2009, pp. 59–64.

[28] R. C. Hibbeler, *Mechanics of Materials*, 8th ed. Upper Saddle River, NJ, USA: Prentice-Hall, 2011.

[29] A. Gray, *Modern Differential Geometry of Curves and Surfaces with Mathematica*. Boca Raton, FL, USA: CRC Press, 2006.

[30] S. Patil, J. Pan, P. Abbeel, and K. Goldberg, "Planning curvature and torsion constrained ribbons in 3D with application to intracavitary brachytherapy," *IEEE Trans. Autom. Sci. Eng.*, vol. 12, no. 4, pp. 1332–1345, Oct. 2015.

[31] *Manual 'ILLumiSense' Software*, document Version 2.3, FBGS International, Bell Telephonelaan 2H, Geel Belgium, 2014.

[32] A. Leibinge, M. J. Oldfield, and F. B. Rodriguez, "Minimally disruptive needle insertion: A biologically inspired solution," *Interface Focus*, vol. 6, no. 3, 2016, Art. no. 20150107.

[33] L. Frasson, F. Ferroni, S. Y. Ko, G. Dogangil, and F. R. Y. Baena, "Experimental evaluation of a novel steerable probe with a programmable bevel tip inspired by nature," *J. Robotic Surg.*, vol. 6, no. 3, pp. 189–197, 2012.